Amplified circularly polarized luminescence promoted by hierarchical self-assembly involving Pt···Pt interactions

Gui-Fei Huo[1†], Qian Tu[1†], Yi-Xiong Hu[1], Bo Jiang[1], Qi-Feng Zhou[1], Yanfei Niu[1], Xiaoli Zhao[1], Hong-Ming Ding[2*], Jin Wen[3,4*], Guang-Qiang Yin[1], Xueliang Shi[1] and Lin Xu[1*]

ABSTRACT The design and construction of highly effective circularly polarized luminescence (CPL)-active materials has aroused considerable attention due to their widespread applications in sensors, optical devices, and asymmetric synthesis. However, the exploration of novel CPL-active materials with high luminescence dissymmetry factor (g_{lum}) values is still a challenge. Herein, we describe a new approach for the preparation of supramolecular metallacycles with amplified CPL promoted by hierarchical self-assembly involving Pt···Pt interactions. Notably, the resultant metallacycles exhibited strong CPL signals with high g_{lum} values, while their corresponding precursors were CPL silent. The CPL amplification mechanism was comprehensively validated by ultraviolet-visible absorption, emission spectroscopy, nuclear magnetic resonance spectroscopy, scanning electron microscopy, transmission electron microscopy, atomic force microscopy, coarse-grained molecular dynamics simulations, and time-dependent density functional theory calculations. This work thus provides the first example of preparing highly effective CPL-active materials based on hierarchical self-assembly involving Pt···Pt interactions.

Keywords: metallacycle, circularly polarized luminescence, hierarchical self-assembly, Pt···Pt interaction

INTRODUCTION

Circularly polarized luminescence (CPL) is a fascinating chiroptical luminescence phenomenon that occurs as a result of the preferential emission of left or right circularly polarized radiation from the chiral excited state of a molecular system [1–6]. During the past decades, the fabrication of CPL-active materials has attracted increasing interest because of the wide applications of such materials in biological chiroptical sensing, three-dimensional (3D) optical display and storage, chiral photoelectric devices, and asymmetric catalytic reactions [7–13]. Usually, the luminescence dissymmetry factor (g_{lum}) value, which is used to quantify the level of CPL, of organic molecules is relatively low and generally within the range of 10^{-5}–10^{-3} due to the large electric dipole transitions [14]. Therefore, achieving a large g_{lum} value is one of the most urgent issues in developing CPL-active materials [15–20]. Many strategies, including the formation of receptor–ion complexes and configurational changes upon binding with guests, have been adopted to amplify the g_{lum} value [21,22]. Notably, nature often forms chiral biosystems by employing a hierarchical self-assembly strategy, in which the components are brought together in a stepwise process *via* multiple noncovalent interactions [23,24]. For instance, the natural system is able to express and amplify molecular chirality into preferred supramolecular α helicity, such as the secondary helical structures of peptides and proteins, through hierarchical self-assembly [25]. Inspired by this, hierarchical self-assembly might be employed to prepare highly effective CPL-active systems since it offers the possibility to fabricate CPL-active materials from not only the chiral luminescent compounds but also completely achiral luminescent molecules through chirality transfer, chirality induction, and symmetry breaking [26–28]. However, compared with many well-known strategies to fabricate CPL-active systems, hierarchical self-assembly has rarely been explored and remains a major challenge.

As one of the most important metallophilic interactions of d8- and d10-metals, Pt···Pt interactions usually allow intriguing spectroscopic and luminescence properties as well as tunable photoluminescence behaviors achieved by modulating the Pt···Pt distances [29–33]. Recently, Pt···Pt interactions have emerged as a key driving force for providing the precise control and tuning of the self-assembly of building blocks into designated supramolecular architectures with high photoluminescent properties [34–37]. Considering that the Pt···Pt interactions usually give rise to the intriguing luminescence properties and plays a critical role in self-assembly, we envisioned that the participation of the Pt···Pt interactions in the fabrication of CPL-active materials would endow the resultant materials with enhanced luminescent properties and interesting hierarchical self-assembly behavior. Very surprisingly, to the best of our knowledge, the fabrication

[1] Shanghai Key Laboratory of Green Chemistry and Chemical Processes, School of Chemistry and Molecular Engineering, East China Normal University, Shanghai 200062, China
[2] Center for Soft Condensed Matter Physics and Interdisciplinary Research, School of Physical Science and Technology, Soochow University, Suzhou 215006, China
[3] China State Key Laboratory for Modification of Chemical Fibers and Polymer Materials & College of Materials Science and Engineering, Donghua University, Shanghai 201620, China
[4] Institute of Theoretical Chemistry, Faculty of Chemistry, University of Vienna, Währinger Str. 17, 1090 Vienna, Austria
[†] These authors contributed equally to this work.
[*] Corresponding authors (emails: dinghm@suda.edu.cn (Ding HM); jinwen@dhu.edu.cn (Wen J); lxu@chem.ecnu.edu.cn (Xu L))

of CPL-active materials through hierarchical self-assembly involving Pt···Pt interactions has not yet been reported.

Herein, we present a successful construction of well-defined chiral metallacycles M-*S* and M-*R* (M represents metallacycle) *via* coordination-driven self-assembly of the chiral alkynyl-platinum(II) dipyridine building blocks L-*S* and L-*R* (L represents ligand), respectively, containing optically active (*S/R*)-3,7-dimethyloctyl groups with di-platinum(II) acceptor (Fig. 1). Interestingly, unlike the building blocks L-*S* and L-*R* that were CPL silent, metallacycles M-*S* and M-*R* displayed strong CPL signals with high g_{lum} values up to 0.014. Comprehensive mechanistic studies revealed that the formation of a metallacycle favored stepwise self-assembly through intermolecular Pt···Pt and π-π stacking interactions, resulting in the formation of nanorods with high CPL activity. This research provides the first successful example of CPL amplification promoted by hierarchical self-assembly involving Pt···Pt interactions.

EXPERIMENTAL SECTION

Materials and instruments

^{1}H nuclear magnetic resonance (NMR), ^{13}C NMR, and ^{31}P NMR spectra were recorded on a Bruker 400 MHz Spectrometer (^{1}H: 400 MHz; ^{13}C: 100 MHz; ^{31}P: 161.8 MHz) or Bruker 500 MHz Spectrometer (^{1}H: 500 MHz; ^{13}C: 125 MHz; ^{31}P: 202.2 MHz) at 298 K. The 2D NMR spectra (^{1}H-^{1}H correlation spectroscopy (COSY), rotating frame overhauser effect spectroscopy (ROESY) and diffusion ordered spectroscopy (DOSY)) were recorded on a Bruker 500 MHz Spectrometer (^{1}H: 500 MHz) at 298 K. The ^{1}H and ^{13}C NMR chemical shifts reported were related to the residual solvent, and ^{31}P NMR resonances were referred to an internal standard sample of 85% H_3PO_4 (δ 0.0). Coupling constants (*J*) were denoted in Hz and chemical shifts (δ) in ppm. Multiplicities were denoted as follows: s = singlet, d = doublet, m = multiplet, br = broad. Electrospray ionization (ESI) mass spectra were recorded with a Waters Synapt G2 mass spectro-

meter. The cold spray ionization time-of-flight mass spectrometry (CSI-TOF-MS) spectra were acquired by using an AccuTOF CS mass spectrometer (JMS-T100CS, JEOL, Tokyo, Japan). Scanning electron microscopy (SEM) images were obtained by using an S-4800 (Hitachi Ltd.) with an accelerating voltage of 10.0 kV. Transmission electron microscopy (TEM) measurements were performed under a Tecnai G2 20 TWIN device. All the atomic force microscopy (AFM) images were obtained on a Dimension FastScan (Bruker), using ScanAsyst mode under ambient condition. Dynamic light scattering (DLS) measurements were conducted under a Malvern Zetasizer Nano-ZS light scattering apparatus (Malvern Instruments, U. K.) with a He-Ne laser (633 nm, 4 mW). Ultraviolet-visible (UV-Vis) spectra were recorded in a quartz cell (light path 10 mm) on a Cary 50Bio UV-Visible spectrophotometer. Fluorescence spectra were carried out using an RF-5301PC spectrophotometer. Circular dichroism (CD) spectra were recorded on a chirascan series Circular Dichroism Spectropolarimeter. CPL measurements were performed with a JASCO CPL-200 spectrometer (light path 0.1 mm). Single crystal X-ray diffraction data were collected on a Rigaku Saturn X-ray diffractometer with graphite-monochromator Mo-Kα radiation (λ = 0.71073 Å) at 173 K. Single crystals suitable for X-ray crystallographic analysis were obtained through slow diffusion of ethanol (EtOH) into dichloromethane (DCM).

Synthesis of L-*S*, L-*R*, L2-*S*, L2-*R*, L3-*S* and L3-*R*

The synthetic methods and the characterizations of L-*S*, L-*R*, L2-*S*, L2-*R*, L3-*S* and L3-*R* are detailed in the Supplementary information (Figs S1–S24 and Table S1).

Coarse-grained molecular dynamics (CGMD) simulations

The CGMD simulations were applied to investigate the underlying mechanism of the self-assembly of the ligand L and the corresponding metallacycle M. For simplicity, we constructed the CG model with different topologies by using the different
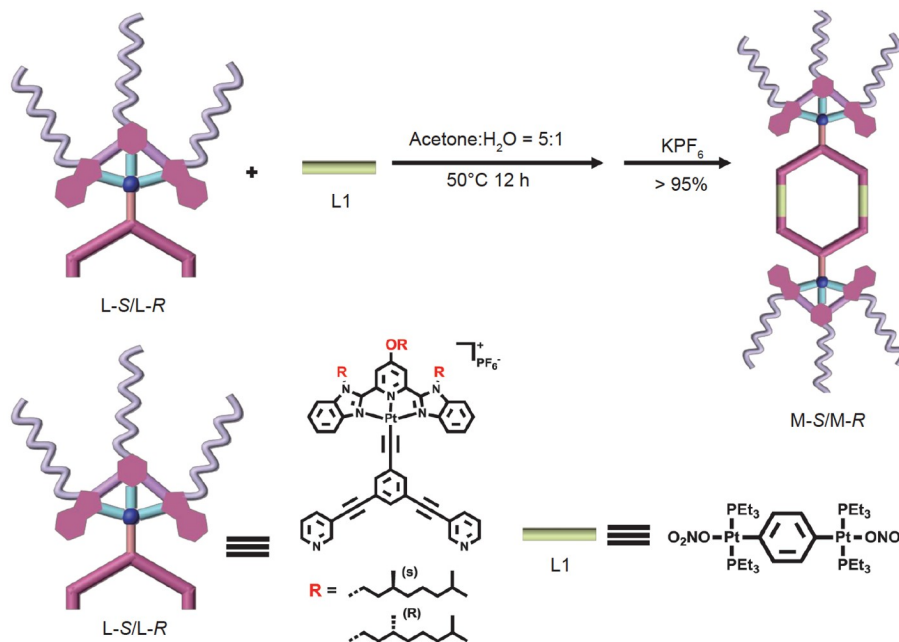
Figure 1 Self-assembly of 0° dipyridyl donor ligands L-*S*/L-*R* and 180° di-Pt(II) acceptor L1 into chiral metallacycles M-*S*/M-*R*.

types of beads (Bz1, Bz2, Pt, S, T beads) to denote the L and M molecules in the simulations.

Time-dependent density functional theory (TD-DFT) calculations
TD-DFT calculations were carried out to simulate the absorption spectra of the monomers at PBE0/def2-SVP level with a resolution of identity (RI) approximation. CD spectra of dimers were simulated at PBE0/def2-SVP level with Grimme's dispersion correction for 160 excited states.

RESULTS AND DISCUSSION

The chiral alkynyl-Pt(II)-containing dipyridine donor ligands L-S and L-R were easily synthesized through the etherification reaction and Sonagashira coupling reaction as shown in the Supplementary information. Chiral hexagonal metallacycles M-S and M-R containing two alkynyl-Pt(II) bzimpy moieties were constructed by simply mixing the corresponding chiral donor ligand L-S or L-R, respectively, with the linear diplatinum(II) acceptor L1 in a molar ratio of 1:1, resulting in a quantitative yield *via* coordination-driven self-assembly. As shown in Figs S25–S32, the structures of the obtained metallacycles M-S and M-R were well characterized by ^{1}H and ^{31}P NMR spectroscopy and ESI-TOF-MS, which revealed the formation of discrete and highly symmetric species. The ^{31}P NMR spectra of the assemblies M-S and M-R displayed a sharp singlet peak (~18.54 ppm) with concomitant ^{195}Pt satellites corresponding to a single phosphorus environment. This charge is consistent with the electron back-donation from the platinum atoms (M-S versus L1 by ~5.07 ppm and M-R versus L1 by ~5.08 ppm). In Figs S33 and S34, ESI-TOF-MS provided additional evidence for the formation of discrete desired metallacycles. The ESI-TOF-MS spectrum of rhomboidal M-S exhibited three peaks at m/z = 903.56, m/z = 1165.50 and m/z = 1602.39, corresponding to the different charge states $[A-5PF_6^-]^{5+}$, $[A-4PF_6^-]^{4+}$ and $[A-3PF_6^-]^{3+}$, respectively, where A represents the intact assemblies. These peaks were isotopically resolved and agreed with the theoretical isotopic patterns. Similarly, peaks that agreed well with the corresponding simulated isotope patterns were found in the mass spectrum of M-R, which allowed the metallacycles to be unambiguously identified.

Due to the existence of the chiral centers and luminescent units, the chiroptical properties of both metallacycles M-S and M-R (5.0×10^{-6} mol L^{-1}) and their building blocks L-S and L-R (1.0×10^{-5} mol L^{-1}) were investigated by CD and CPL in DCM:

hexane (50:50 v/v) at 298 K under the ambient conditions. As shown in Fig. 2a, metallacycles M-S and M-R exhibit obvious mirror-image CD signals with a crossover at 300 nm, while their corresponding building blocks L-S and L-R are CD silent. In addition, we also measured their CD spectra at different volume ratios of DCM/hexane to study the supramolecular chirality. In the case of M-S and L-S, the CD spectra of M-S obtained in DCM:hexane (v/v) = 60:40, 50:50, 40:60, and 30:70 clearly showed a Cotton effect. However, the samples of other volume ratios were almost CD silent (Fig. S35a). For L-S, there was no CD signal observed under any conditions (Fig. S35b). Compared with the CD response, CPL is a unique property pertaining to the excited-state of a chiral system. In Fig. S36, no obvious CPL signal could be detected for the building blocks L-S in DCM/hexane solution. Unexpectedly, metallacycles M-S showed strong negative signals at 600 nm, whereas M-R exhibited the opposite signals at the same wavelength (Fig. 2b). In a same manner, the CPL spectra of the self-assemblies at different volume ratios of DCM/hexane were also investigated. Nevertheless, there was no CPL signal for L-S and L-R, while the signal of M-S was exclusively found in DCM:hexane (50:50 v/v) (Fig. S37a, S37b). Moreover, the calculated g_{lum} values of CPL were approximately 0.014 for both metallacycles M-S and M-R, larger than any of previously CPL-active materials [38,39]. These results clearly indicated that the CPL signals were significantly enhanced through the formation of supramolecular metallacycles.

In order to gain deep insight into CPL amplification upon the formation of supramolecular metallacycles, the UV-Vis absorption and emission spectra of metallacycles M-S and M-R with the ligands L-S and L-R in DCM/hexane of different volume ratios were recorded. In Fig. S38, the absorption spectra of metallacycles M-S and M-R and their ligands L-S and L-R displayed intense intraligand (IL) absorption bands at λ = 261–333 nm and weak absorption bands at λ = 381–450 nm in DCM. The low-energy absorption bands were attributed to a metal-to-ligand charge-transfer (MLCT) transition together with a ligand-to-ligand charge-transfer (LLCT) transition [40]. As shown in Fig. 3a and Fig. S39a, with the gradual addition of hexane into the solutions, a gradual decrease in the intensity of the absorption band at λ = 350 nm and a concomitant growth of an absorption tail at $\lambda \sim$ 500 nm were observed for metallacycle M-S or M-R when the volume fraction of hexane was less than 40%. It was noteworthy that the low-energy absorption tail at $\lambda \sim$
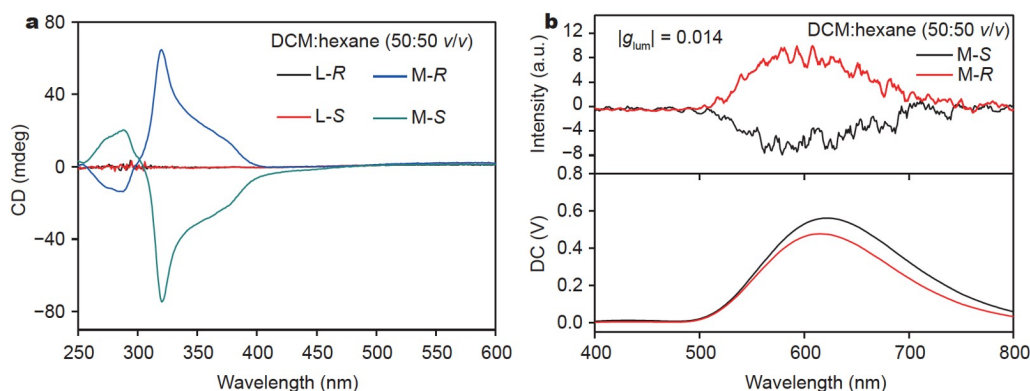
Figure 2 (a) CD spectra of L-S/L-R (1.0×10^{-5} mol L^{-1}) and M-S/M-R (5.0×10^{-6} mol L^{-1}) in DCM:hexane (50:50 v/v). (b) CPL spectra (excited at λ = 330 nm) of M-S and M-R in DCM:hexane (50:50 v/v) at room temperature.
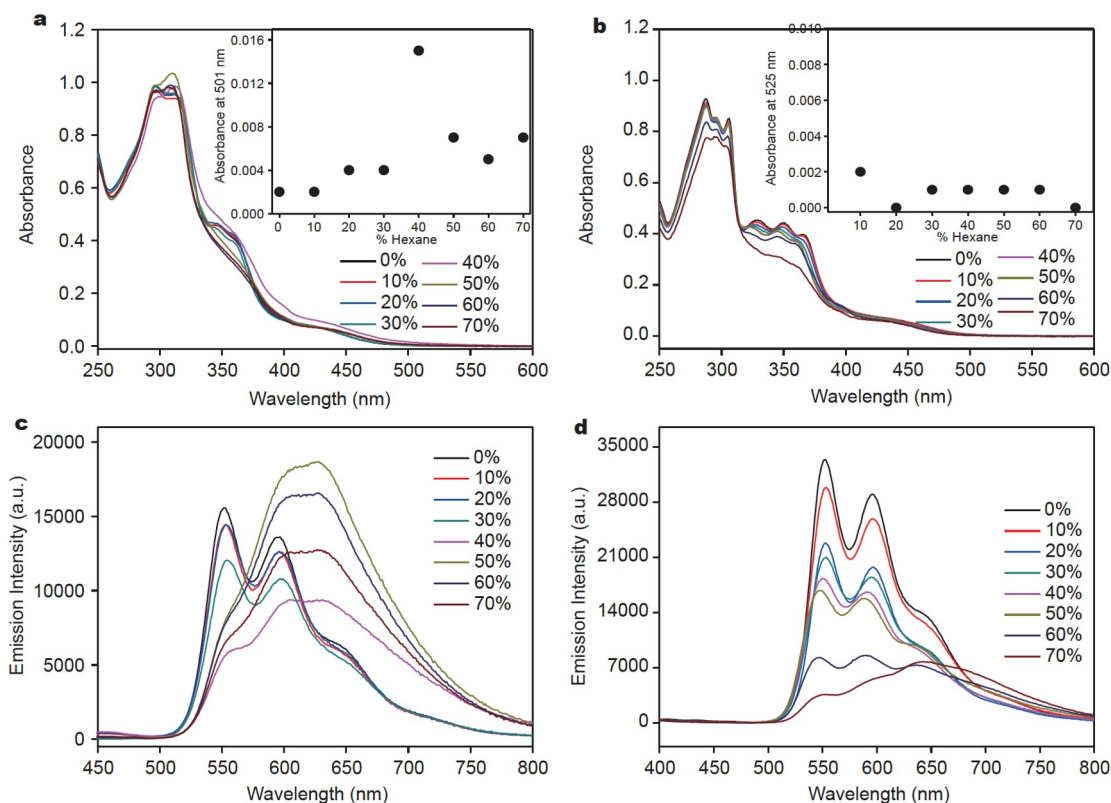
Figure 3 UV-Vis absorption spectra of (a) M-*S* (5.0×10^{-6} mol L^{-1}) and (b) L-*S* (1.0×10^{-5} mol L^{-1}) in DCM upon increasing the hexane content (insets: plots of absorbance *versus* volume percentage of hexane). Emission spectra (excited at $\lambda = 420$ nm) of (c) M-*S* (5.0×10^{-6} mol L^{-1}) and (d) L-*S* (1.0×10^{-5} mol L^{-1}) in DCM upon increasing the hexane content.

500 nm could be usually attributed to a typical metal-metal-to-ligand charge-transfer (MMLCT) transition, which is related to intermolecular Pt···Pt and π-π stacking interactions [41]. Surprisingly, a further increase in the percentage of hexane fraction from 40% to 70% resulted in a reduction for the low-energy absorption tail at $\lambda \sim 500$ nm for M-*S* and M-*R*. This indicated the metallacycles M-*S* and M-*R* underwent an aggregation-partial disaggregation process when the *n*-hexane fraction was increased from 0% to 70% [41,42]. In contrast, for the ligands L-*S* and L-*R*, a gradual decrease in the intensity of the absorption band at $\lambda = 329$ nm and nearly no change in the low-energy absorption tail at $\lambda \sim 500$ nm were observed as the hexane fraction increased, implying that the ligands L-*S* and L-*R* could not form Pt···Pt or π-π stacking interactions even when the *n*-hexane fraction was increased to 70% (Fig. 3b and Fig. S39b). On the other hand, the emissions of the ligands L-*S* and L-*R* at $\lambda_{\max}$ = 551 nm, corresponding to the emission of the monomeric Pt(II) bzimpy complex, were gradually quenched upon increasing the *n*-hexane fraction from 0% to 70%, while the emission spectra of the metallacycles M-*S* and M-*R* displayed a significant redshift of the emission maxima from 552 to 627 nm under the same conditions (Fig. 3c, 3d and Fig. S39c, S39d) [43]. This result further indicated that Pt···Pt interactions occurred only in the metallacycles M-*S* and M-*R* but not in the ligands L-*S* and L-*R*. All obtained data demonstrated that the Pt···Pt interactions played a crucial role in the hierarchical self-assembly of the metallacycles M-*S* and M-*R*.

To obtain more detailed information concerning the hierarchical self-assembly, the concentration-dependent and sol-vent-dependent ^{1}H NMR spectra of the representative metallacycle M-*S* were acquired. As shown in Fig. S40, upon increasing the concentration of [D$_{14}$] *n*-hexane, remarkable downfield shifts of the pyridine protons H$_1$ and H$_4$ as well as the up-field shifts of the phenyl protons H$_7$ and H$_{10}$ were observed, indicating the formation of π-π stacking interactions upon the generation of aggregates *via* hierarchical self-assembly. In Fig. S41, the concentration-dependent ^{1}H NMR spectra of M-*S* undoubtedly further supported the existence of π-π stacking interactions. To elucidate the plausible packing arrangements, the ^{1}H-^{1}H NOESY NMR spectrum of the M-*S* (5.0×10^{-4} mol L^{-1}) in CD$_2$Cl$_2$ upon addition of [D$_{14}$] *n*-hexane was recorded. As shown in Fig. S42, the observation of the cross peaks between the signals of H$_{14}$ and H$_6$ and between those of H$_{14}$ and H$_9$ confirmed the presence of π-π stacking that brought the protons into vicinity [42,44]. Furthermore, these newly observed cross peaks suggested that the adjacent metallacycles were probably arranged in a head-to-tail packing form with a slightly staggered structure along the Pt···Pt chain to minimize the steric hindrance between the long chiral alkyl chain and the bulky triethylphosphine units.

The morphologies of the assemblies of the ligands L-*S* and L-*R* and those of the metallacycles M-*S* and M-*R* were observed by using SEM, TEM, and AFM. The SEM, TEM, and AFM images revealed that L-*S* and L-*R* formed uniform nanovesicles in a diameter of approximately 500 nm (Fig. 4a, b and Fig. S43). The thickness of the observed nanovesicles was determined to be ~33.4 nm from the TEM images, implying that they were multi-layered vesicles. In contrast, metallacycles M-*S* and M-*R* were
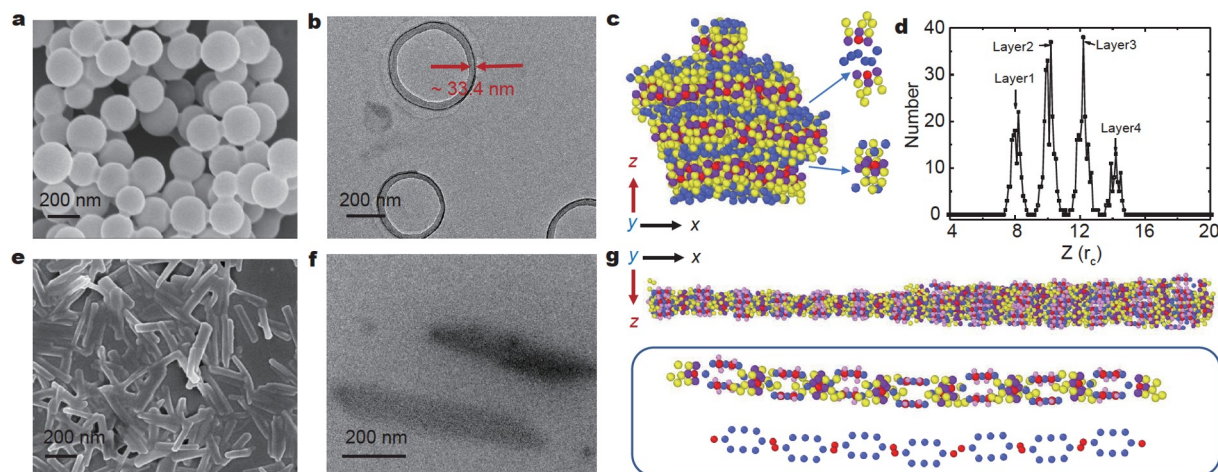
Figure 4 SEM and TEM images of (a, b) L-*S* (1.0×10^{-5} mol L^{-1}) and (e, f) M-*S* (5.0×10^{-6} mol L^{-1}) in DCM:hexane (50:50 *v/v*). (c) A typical equilibrium snapshot of the assembled structure of the ligand L in the simulation. The inset shows the particular packing styles in the multi-layered structure (top: inter-layer packing; down: intra-layer packing). (d) The distribution of the number of Pt beads along the *z* direction in the simulation. (g) A typical equilibrium snapshot of the assembled structure of metallacycle M in the simulation. The snapshots in the box display the particular packing style in the assembly.

self-assembled into nanorods with a length of approximately 600 nm (Fig. 4e, f and Fig. S44). DLS experiments were also conducted to verify the identity of the aggregate species for L-*S* and M-*S*. Fig. S45 shows that the average hydrodynamic diameters (D_h) were 476.3 nm for L-*S*, 546.2 nm for M-*S*, 460.6 nm for L-*R*, and 522.7 nm for M-*R* in DCM/hexane, consistent with the SEM and TEM images. To provide more insights into the distinct morphology of the aggregates, CGMD simulations were applied to investigate the self-assembly process of the ligand L and its corresponding metallacycle M. In the simulation, L and M were modelled through the CG method, where each unit in the molecules was represented by using one CG bead (Fig. S46). As shown in Fig. S47, hundreds of L molecules were first randomly placed in the simulation box. Due to the effective interaction among the aromatic rings and the alkaline tails, several L molecules quickly packed together mainly in a head-to-tail conformation and formed the aggregates. Subsequently, these aggregates gradually turned into the regular and layered structures. Interestingly, due to the π-π stacking between the head beads, the aggregates finally adopted a multi-layered structure (Fig. 4c and d). In Fig. S48, since the interaction in the *xy* plane was much stronger than that in the *z* direction, the ligand L was preferentially grown into a layered structure, which consisted with the multi-layered vesicle in the experiment. On the contrary, the linear growth of the M molecules was observed in the simulations (Fig. 4g and Fig. S49). As shown in Fig. S50, despite the existence of the interactions between the aromatic rings (that induced the in-plane growth), the Pt⋯Pt interactions (in the *z* direction) dominated the self-assembly process, leading to the rod-like aggregates in the assembly. Notably, owing to the existing steric hindrance between the alkane tails (i.e., T beads) and the PEt₃ (i.e., S beads), some misplacement between the neighbouring metallacycles occurred. Thus, the linear growth was not ideal, where the symmetry of M arrangement was slightly broken in the nanorods. The distinct morphologies of the ligands and the metallacycles might result in their different CPL properties since the molecular arrangements of the ligands were more symmetric than those of the metallacycles.

The investigation into the chirality properties of the molecules might shed some light onto the CPL mechanism. To explain the role of the Pt⋯Pt interactions involved in the CPL amplification process, attempts to obtain X-ray-quality single crystals of L and M were frustrated. Fortunately, yellow crystals of the precursor compound L2-*S* were obtained for the X-ray diffraction, which was cultivated in a DCM/EtOH solution, similar to other alkynylplatinum(II) complexes [45,46]. From the X-ray crystallographic analysis, the dimeric structure of the L2-*S* complex was observed in a head-to-tail packing arrangement with "short" and "long" Pt⋯Pt distances of 4.752 and 8.540 Å, respectively (Fig. 5a). The Pt⋯Pt distances implied that the Pt⋯Pt interaction was negligible since the efficient Pt⋯Pt interactions should be within the range of 3.09–3.50 Å, as was determined in the previous reports [47,48]. On the other hand, the centroid-to-centroid distances (3.514, 3.619, and 3.482 Å) indicated that the intermolecular π-π interaction played a significant role in this molecule (Fig. 5b). The chiral alkyl chains were centrosymmetric in the head-to-tail dimer, resulting in relatively weak CD signals, consistent with the corresponding UV-Vis and CD spectra (Fig. S51). Additionally, two models, La and Ma (Fig. S52), were generated to simulate the absorption spectra of L and M by TD-DFT calculations (Figs S53–S55), and the results were in good agreement with the experimental absorption spectra. Since the Pt-PEt₃ groups did not contribute to the electronic transitions in the lower excited states (Figs S56 and S57, Tables S2 and S3), M could be further simplified as La to investigate the electronic structure in the excited states of its dimer. The CD spectra were simulated by TD-DFT calculations in four models, L-*S*, L-*R*, M-*S*, and M-*R*, in which the dimers were stacked in different orientations with the Pt atoms face-to-face, as shown in Fig. 5c. The simulated CD spectra demonstrated that the chirality of the Pt⋯Pt interaction-driven self-assembled M was enhanced when the crossing angles of the dipole moments increased from 0° to 90° (Figs S58 and S59). In Fig. S60, the differences between the simulated spectra and the experimental measurements were possibly due to the effect of solvents. Moreover, the models of L-*S* and L-*R* agreed well with the crystal structure of L2-*S*, in which
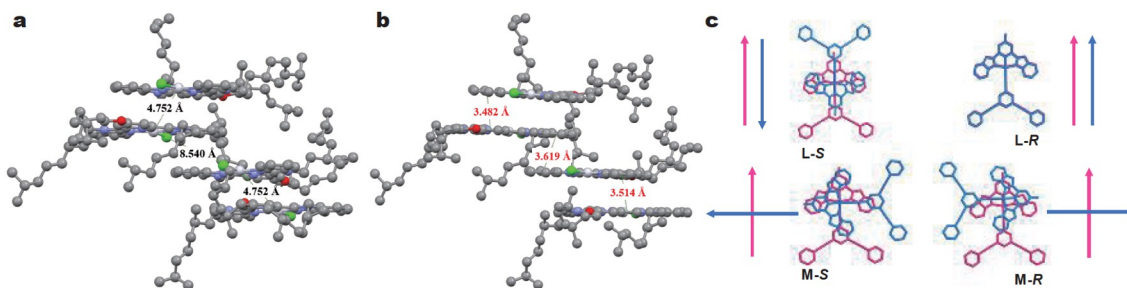
Figure 5 (a, b) The crystal packing of L2-*S*. PF_6^- anions were omitted for clarity (the short and long Pt···Pt distances were 4.752 and 8.540 Å, respectively; the π-π distances were measured as 3.514, 3.619, and 3.482 Å). (c) The TD-DFT-simulated dipole moments of the monomers.

the dipole moments of the dimers were parallel or anti-parallel to one another.

CONCLUSIONS

In summary, two well-defined chiral metallacycles M-*S* and M-*R*, which could form the highly effective CPL-active materials through hierarchical self-assembly involving Pt···Pt interactions, were constructed in this work. In contrast to their precursors, which were CPL silent, they were found as prominent CPL-active materials with a high g_{lum} value of up to 0.014. The mechanistic studies revealed that the intermolecular Pt···Pt interaction played a significant role in CPL signal amplification. This work not only provides a facile approach to the fabrication of highly effective CPL-active materials, but also offers a new strategy for the design and preparation of other chiroptical materials based on transition-metal complexes featuring metallophilic interactions.

1 Sang Y, Han J, Zhao T, *et al.* Circularly polarized luminescence in nanoassemblies: Generation, amplification, and application. Adv Mater, 2019, 32: 1900110

2 Carr R, Evans NH, Parker D. Lanthanide complexes as chiral probes exploiting circularly polarized luminescence. Chem Soc Rev, 2012, 41: 7673–7686

3 Li M, Wang YF, Zhang D, *et al.* Axially chiral TADF-active enantiomers designed for efficient blue circularly polarized electroluminescence. Angew Chem Int Ed, 2020, 59: 3500–3504

4 Sun Y, Li S, Zhou Z, *et al.* Alanine-based chiral metallogels *via* supramolecular coordination complex platforms: Metallogelation induced chirality transfer. J Am Chem Soc, 2018, 140: 3257–3263

5 Yang JG, Li K, Wang J, *et al.* Controlling metallophilic interactions in chiral gold(I) double salts towards excitation wavelength-tunable circularly polarized luminescence. Angew Chem Int Ed, 2020, 59: 6915–6922

6 Schulte TR, Holstein JJ, Krause L, *et al.* Chiral-at-metal phosphorescent square-planar Pt(II)-complexes from an achiral organometallic ligand. J Am Chem Soc, 2017, 139: 6863–6866

7 Han J, Guo S, Lu H, *et al.* Recent progress on circularly polarized luminescent materials for organic optoelectronic devices. Adv Opt Mater, 2018, 6: 1800538

8 Zhang DW, Li M, Chen CF. Recent advances in circularly polarized electroluminescence based on organic light-emitting diodes. Chem Soc Rev, 2020, 49: 1331–1343

9 Li M, Wang YF, Zhang DW, *et al.* Thermally activated delayed fluorescence material-sensitized helicene enantiomer-based OLEDs: a new strategy for improving the efficiency of circularly polarized electroluminescence. Sci China Mater, 2021, 64: 899–908

10 Zinna F, Pasini M, Galeotti F, *et al.* Design of lanthanide-based OLEDs with remarkable circularly polarized electroluminescence. Adv Funct Mater, 2017, 27: 1603719

11 Zhou Y, Li H, Zhu T, *et al.* A highly luminescent chiral tetrahedral $Eu_4L_4(L')_4$ cage: Chirality induction, chirality memory, and circularly polarized luminescence. J Am Chem Soc, 2019, 141: 19634–19643

12 Takaishi K, Iwachido K, Takehana R, *et al.* Evolving fluorophores into circularly polarized luminophores with a chiral naphthalene tetramer: Proposal of excimer chirality rule for circularly polarized luminescence. J Am Chem Soc, 2019, 141: 6185–6190

13 Shuvaev S, Fox MA, Parker D. Monitoring of the ADP/ATP ratio by induced circularly polarised europium luminescence. Angew Chem Int Ed, 2018, 57: 7488–7492

14 Ma K, Chen W, Jiao T, *et al.* Boosting the circularly polarized luminescence of small organic molecules *via* multi-dimensional morphology control. Chem Sci, 2019, 10: 6821–6827

15 Nakamura K, Furumi S, Takeuchi M, *et al.* Enantioselective synthesis and enhanced circularly polarized luminescence of S-shaped double azahelicenes. J Am Chem Soc, 2014, 136: 5555–5558

16 Park G, Kim H, Yang H, *et al.* Amplified circularly polarized phosphorescence from co-assemblies of platinum(II) complexes. Chem Sci, 2019, 10: 1294–1301

17 Han J, Yang D, Jin X, *et al.* Enhanced circularly polarized luminescence in emissive charge-transfer complexes. Angew Chem Int Ed, 2019, 58: 7013–7019

18 Yang D, Duan P, Zhang L, *et al.* Chirality and energy transfer amplified circularly polarized luminescence in composite nanohelix. Nat Commun, 2017, 8: 15727

19 Li Y, Liu K, Li X, *et al.* The amplified circularly polarized luminescence regulated from D–A type AIE-active chiral emitters *via* liquid crystals system. Chem Commun, 2020, 56: 1117–1120

20 Zhao J, Zhang T, Dong XY, *et al.* Circularly polarized luminescence from achiral single crystals of hybrid manganese halides. J Am Chem Soc, 2019, 141: 15755–15760

21 Maeda H, Bando Y, Shimomura K, *et al.* Chemical-stimuli-controllable circularly polarized luminescence from anion-responsive π-conjugated molecules. J Am Chem Soc, 2011, 133: 9266–9269

22 Haketa Y, Bando Y, Takaishi K, *et al.* Asymmetric induction in the preparation of helical receptor-anion complexes: Ion-pair formation with chiral cations. Angew Chem Int Ed, 2012, 51: 7967–7971

23 Aggeli A, Nyrkova IA, Bell M, *et al.* Hierarchical self-assembly of chiral rod-like molecules as a model for peptide-sheet tapes, ribbons, fibrils, and fibers. Proc Natl Acad Sci U S A, 2001, 98: 11857–11862

24 Yang Y, Liang J, Pan F, *et al.* Macroscopic helical chirality and self-motion of hierarchical self-assemblies induced by enantiomeric small molecules. Nat Commun, 2018, 9: 3808

25 Song Z, Fu H, Wang R, *et al.* Secondary structures in synthetic polypeptides from *N*-carboxyanhydrides: design, modulation, association, and material applications. Chem Soc Rev, 2018, 47: 7401–7425

26 Ikai T, Okubo M, Wada Y. Helical assemblies of one-dimensional supramolecular polymers composed of helical macromolecules: Generation of circularly polarized light using an infinitesimal chiral source. J

Am Chem Soc, 2020, 142: 3254–3261

27 Zhang J, Liu Q, Wu W, et al. Real-time monitoring of hierarchical self-assembly and induction of circularly polarized luminescence from achiral luminogens. ACS Nano, 2019, 13: 3618–3628

28 Watanabe K, Iida H, Akagi K. Circularly polarized blue luminescent spherulites consisting of hierarchically assembled ionic conjugated polymers with a helically π-stacked structure. Adv Mater, 2012, 24: 6451–6456

29 Wong KMC, Yam VWW. Self-assembly of luminescent alkynyl-platinum(II) terpyridyl complexes: modulation of photophysical properties through aggregation behavior. Acc Chem Res, 2011, 44: 424–434

30 Han Y, Gao Z, Wang C, et al. Recent progress on supramolecular assembly of organoplatinum(II) complexes into long-range ordered nanostructures. Coord Chem Rev, 2020, 414: 213300

31 Koo CK, Lam B, Leung SK, et al. A "molecular pivot-hinge" based on the pH-regulated intramolecular switching of Pt–Pt and π-π interactions. J Am Chem Soc, 2006, 128: 16434–16435

32 Zhang X, Ao L, Han Y, et al. Modulating Pt···Pt metal–metal interactions through conformationally switchable molecular tweezer/guest complexation. Chem Commun, 2018, 54: 1754–1757

33 Jiang B, Zhang J, Ma JQ, et al. Vapochromic behavior of a chair-shaped supramolecular metallacycle with ultra-stability. J Am Chem Soc, 2016, 138: 738–741

34 Wang X, Han Y, Liu Y, et al. Cooperative supramolecular polymerization of fluorescent platinum acetylides for optical waveguide applications. Angew Chem Int Ed, 2017, 56: 12466–12470

35 Aliprandi A, Mauro M, De Cola L. Controlling and imaging biomimetic self-assembly. Nat Chem, 2016, 8: 10–15

36 Wong VCH, Po C, Leung SYL, et al. Formation of 1D infinite chains directed by metal–metal and/or π-π stacking interactions of water-soluble platinum(II) 2,6-bis(benzimidazol-2′-yl)pyridine double complex salts. J Am Chem Soc, 2018, 140: 657–666

37 Jiang B, Chen LJ, Yin GQ, et al. Multiphase transition of supramolecular metallogels triggered by temperature. Chem Commun, 2017, 53: 172–175

38 Peeters E, Christiaans MPT, Janssen RAJ, et al. Circularly polarized electroluminescence from a polymer light-emitting diode. J Am Chem Soc, 1997, 119: 9909–9910

39 Oyama H, Nakano K, Harada T, et al. Facile synthetic route to highly luminescent sila[7]helicene. Org Lett, 2013, 15: 2104–2107

40 Tam AYY, Wong KMC, Yam VWW. Unusual luminescence enhancement of metallogels of alkynylplatinum(II) 2,6-bis(N-alkylbenzimidazol-2′-yl)pyridine complexes upon a gel-to-sol phase transition at elevated temperatures. J Am Chem Soc, 2009, 131: 6253–6260

41 Po C, Tam AYY, Wong KMC, et al. Supramolecular self-assembly of amphiphilic anionic platinum(II) complexes: a correlation between spectroscopic and morphological properties. J Am Chem Soc, 2011, 133: 12136–12143

42 Fu HLK, Po C, Leung SYL, et al. Self-assembled architectures of alkynylplatinum(II) amphiphiles and their structural optimization: A balance of the interplay among Pt···Pt, π–π stacking, and hydrophobic–hydrophobic interactions. ACS Appl Mater Interfaces, 2017, 9: 2786–2795

43 Jiang B, Zhang J, Zheng W, et al. Construction of alkynylplatinum(II) bzimpy-functionalized metallacycles and their hierarchical self-assembly behavior in solution promoted by Pt···Pt and π-π interactions. Chem Eur J, 2016, 22: 14664–14671

44 Ni J, Zhang LY, Wen HM, et al. Luminescence vapochromic properties of a platinum(II) complex with 5,5′-bis(trimethylsilylethynyl)-2,2′-bipyridine. Chem Commun, 2009, 3801

45 Wan Q, Xiao XS, To WP, et al. Counteranion- and solvent-mediated chirality transfer in the supramolecular polymerization of luminescent platinum(II) complexes. Angew Chem Int Ed, 2018, 57: 17189–17193

46 Yam VWW, Wong KMC, Zhu N. Solvent-induced aggregation through metal···metal/π···π interactions: Large solvatochromism of luminescent organoplatinum(II) terpyridyl complexes. J Am Chem Soc, 2002, 124: 6506–6507

47 Lu W, Zhu N, Che CM. Tethered trinuclear cyclometalated platinum(II) complexes: from crystal engineering to tunable emission energy. Chem Commun, 2002, 900–901

48 Lu W, Chan MCW, Zhu N, et al. Structural and spectroscopic studies on Pt···Pt and π−π interactions in luminescent multinuclear cyclometalated platinum(II) homologues tethered by oligophosphine auxiliaries. J Am Chem Soc, 2004, 126: 7639–7651

Author contributions Xu L conceived the project and wrote the manuscript. Huo GF and Tu Q performed the most of the experiments. Ding HM and Wen J carried out the calculation. Hu YX, Jiang B, Zhou QF and Yin GQ helped with the experiments and data analyses. Niu Y, Zhao X and Shi X revised the manuscript. All authors contributed to the general discussion.

Conflict of interest The authors declare that they have no conflict of interest.

Supplementary information Experimental details and supporting data are available in the online version of the paper.

Gui-Fei Huo received his Doctor's degree at the School of Chemistry and Molecular Engineering, East China Normal University (ECNU) in 2020. He is currently a postdoctoral research fellow at the National University of Singapore under the guidance of Prof. Jishan Wu. His research focuses on supramolecular chemistry and radical chemistry.

Qian Tu received her Bachelor's degree at the School of Chemistry, Sichuan University in 2018. She is now a graduate student at the ECNU, wherein she focuses on supramolecular radical chemistry supervised by Prof. Hai-Bo Yang.

Hong-Ming Ding received his BS degree in 2010 and PhD degree in 2015 from Nanjing University. He is currently a professor at the Center for Soft Condensed Matter Physics and Interdisciplinary Research, Soochow University. His research interests mainly include the understanding of cell-nanoparticle interactions and the protein corona of nanoparticles, as well as the self-assembly of biomolecules/polymers by using multiscale molecular simulations.

Jin Wen is a professor at Donghua University. She received her PhD degree in chemistry from Nanjing University under the supervision of Prof. Jing Ma in 2012. Then she was appointed as an associate scientist at the Academy of Sciences of the Czech Republic, and a project leader at the University of Vienna until 2020. Her interests focus on the theoretical investigation of ultrafast processes in photochemistry and photophysics, such as singlet fission in the dye-sensitized solar cell and molecular machines.

Lin Xu received his PhD degree in chemistry from the ECUST in 2012 under the supervision of Professor Xuhong Qian. Subsequently, he joined the ECNU as an assistant professor and was promoted to associate professor and full professor in 2014 and 2018, respectively. He carried out two years postdoctoral research at the University of Cambridge with Prof. Jonathan Nitschke during 2015–2017. His research interests mainly focus on the supramolecular fluorescent chemistry.

铂···铂相互作用诱导逐级自组装促进圆偏振光信号放大

霍桂飞[1†]，涂倩[1†]，胡毅雄[1]，江波[1]，周启峰[1]，牛艳霏[1]，赵小莉[1]，丁泓铭[2*]，闻瑾[3,4*]，尹光强[1]，史学亮[1]，徐林[1*]

摘要 高效圆偏振发光材料在传感、光学器件、不对称合成等领域有着广泛的应用，设计和制备圆偏振发光材料引起了人们的广泛关注. 然而，构筑具有高发光不对称因子的圆偏振发光材料仍然是一个挑战. 这里，我们制备了一种手性超分子组装金属大环，该超分子组装金属大环可以通过分子间铂···铂相互作用诱导逐级自组装促进圆偏振光的放大. 值得注意的是，超分子组装金属大环显示出高的发光不对称因子以及较强的圆偏振光信号，而其对应的组装配体没有显示出圆偏振光信号. 通过紫外-可见吸收光谱和发射光谱、核磁共振氢谱、扫描电镜、透射电镜、原子力显微镜、粗粒化分子动力学模拟和含时密度泛函理论计算等手段对圆偏振光放大的机理进行了研究. 该研究展示了第一例基于铂···铂相互作用驱动的逐级自组装策略制备的高效圆偏振发光材料.